Dalton Transactions

ROYAL SOCIETY OF CHEMISTRY

PAPER

View Article Online
View Journal | View Issue

Cite this: *Dalton Trans.*, 2025, **54**, 6957

Removal of dibenzothiophene by extraction and catalytic oxidation using long- and short-channel SBA-15 containing Zr and Mo species

Katarzyna Stawicka, * Maciej Trejda, Aleksandra Rybka and Maria Ziolek

Two different SBA-15 silicas with long and short channels, containing zirconium species, were prepared and used as supports for molybdenum additives. The resulting materials were characterized and tested as catalysts for extractive catalytic oxidative desulfurization (ECODS) of dibenzothiophene (DBT) using acetonitrile as a solvent and H_2O_2 as an oxidant. The synthesis procedure for the zirconium-containing silicas influenced both the zirconium loading and its distribution, *i.e.*, whether it was incorporated into the framework or present in extra-framework positions. Additionally, the choice of support for molybdenum inclusion affected the amount of modifier loaded and its resistance to leaching, which collectively impacted the acidic and basic properties of the synthesized catalysts. The textural and surface properties of the materials were evaluated using low-temperature nitrogen adsorption/desorption, XRD, SEM-EDS, FT-IR-ATR, XPS, and UV-vis. The acidity and basicity of the samples were evaluated using FT-IR spectroscopy with pyridine adsorption/desorption and test reactions including 2-propanol dehydration/dehydrogenation and 2,5-hexanedione cyclization/dehydration. The catalytic activity was measured in ECODS. The Mo/ZrSBA-15-S catalyst demonstrated the best performance in DBT removal from the oil phase, achieving approximately 92% conversion of DBT within 120 minutes at 60 °C. This superior activity was attributed to the material's high acidity strength.

Received 7th January 2025,
Accepted 18th March 2025

DOI: 10.1039/d5dt00043b

rsc.li/dalton

1. Introduction

Mesoporous SBA-15 type silica has been widely used as a support for various active components, such as metals, metal oxides, and organosilanes,[1–7] due to its large surface area and narrow pore size distribution. Conventional SBA-15 consists of rod-like channels with micropores located in the silica walls, which contribute to its high hydrothermal stability. Modifications in the SBA-15 synthesis procedure can result in diverse silica morphologies, expanding its potential applications. To date, SBA-15 silicas with morphologies such as spheres, fibers, rods, plates, and rice-like grains have been developed by altering synthesis conditions, such as the temperature, the choice of silica sources, or the addition of specific metal ions, *e.g.*, Sn^{2+} or Zr^{4+}, to the synthesis gel.[7–9]

The platelet structure of short-channel SBA-15 distinctly differs from that of conventional SBA-15, which features a rod-like shape and extended mesochannels. The morphological differences between short- and long-channel SBA-15 are due to the influence of Zr(IV) species within the synthesis gel of platelet SBA-15. When zirconium species are included in the silica synthesis mixture, the average radius of Pluronic P123 micelles increases. This occurs due to the salting out effect, where well-solvated species lower the critical micelle concentration (cmc) of the P123 triblock copolymer and likely boost the local TEOS concentration around P123 micelles. Consequently, the hydrolysis and condensation of TEOS on P123 micelles are sped up by introducing Zr(IV) ions into the synthesis solution. Furthermore, Zr(IV) species might form a dative bond with the hydrophilic PEO chains of P123, which accounts for the predominant presence of zirconium species on the surface of the pore walls.[10] The choice of silica source and the duration of stirring after its incorporation into the synthesis gel influence the morphology of SBA-15 platelets. In the presence of Zr^{4+} ions, TMOS undergoes faster hydrolysis than TEOS, which can lead to quicker silicate condensation at the ends of the copolymer micellar rods, causing earlier termination of platelet SBA-15 growth. Additionally, a shorter stirring time that still allows for TMOS to hydrolyze and dissolve in the synthesis solution enables platelets to grow under static conditions, avoiding interconnections between platelets.[11] Furthermore, the presence of zirconium species during the synthesis enables the formation of Lewis and Brønsted acid sites on the

Adam Mickiewicz University, Poznań, Faculty of Chemistry, Department of Heterogeneous Catalysis, Uniwersytetu Poznańskiego 8, 61-614 Poznań, Poland. E-mail: katarzyna.stawicka@amu.edu.pl; Tel: +48 61 8291795

surface of Zr–SBA-15, provided sulfuric acid is not added at the final stage of the synthesis protocol.[7] When this short-channel SBA-15 is used as a support for additional metal precursors, the interactions between the metallic modifiers and the zirconium species embedded in the silica framework must also be considered.

For long-channel SBA-15, where no Zr(IV) species are added to the synthesis gel, silica-coated P123 micelles are formed once TEOS is added to the synthesis solution. As silica starts to condense, disordered structures and P123 aggregates of the silica nanocomposite materials are created. As the condensation of silicate continues around the P123 micelles, these micelles become elongated and align themselves in a 2D hexagonal pattern. The short rods connect at the channel ends, forming longer rods in the direction of the channels as the reaction continues.[10]

The removal of sulfur compounds from fuel feedstocks and petrochemicals is increasingly important due to the harmful effects of sulfur oxides, produced during the combustion of fossil fuels, on human health and the environment. The method currently employed for the commercial removal of sulfur compounds from crude oil is hydrodesulfurization (HDS). However, this process is not efficient in removing larger sulfur compounds, such as dibenzothiophene (DBT), from fuels. Consequently, alternative methods for sulfur removal from crude oil are needed. According to the literature, several methods as alternatives to HDS have been developed to achieve ultra-low sulfur fuels. These include oxidative desulfurization (ODS), adsorptive desulfurization, and extraction. Among these, ODS appears to be the most attractive option due to its mild reaction conditions and the use of hydrogen peroxide, a so-called "green" oxidant. In the ODS process, sulfur compounds are oxidized sequentially: first to sulfoxides and then directly to sulfones, which exhibit higher polarity. However, the resulting sulfones remain in the reaction mixture and must be separated. This is typically achieved using a polar solvent to extract the sulfones, as their polarity makes them more easily separable than DBT. To streamline the process, it is logical to combine ODS and extraction into a single step, known as extractive catalytic oxidative desulfurization (ECODS). In this integrated approach, sulfur compounds are oxidized to sulfones and simultaneously removed from crude oil through an extraction technique.[12–14]

According to the literature, catalysts exhibiting good activity in oxidative desulfurization (ODS) should possess Brønsted acid sites[15,16] and/or active species capable of interacting with hydrogen peroxide. To date, transition metals have been predominantly used as active centers for such interactions with hydrogen peroxide. These include titanium,[17,18] tungsten,[19,20] molybdenum,[1,21,22] and vanadium.[23–25]

In light of the data presented above, the aim of this work was to synthesize two SBA-15 materials with distinct morphologies: rod-like (long-channel) and plate-like (short-channel), to be used as supports for zirconium and molybdenum species. To the best of our knowledge, no data exist in the literature on the effect of zirconium species retained in short-channel SBA-15 on the performance of molybdenum supported on its surface. It was hypothesized that these catalysts would exhibit enhanced effectiveness due to interactions between zirconium species and pseudo-bridging Si–O(H)···Mo(=O)$_2$ moieties. The study focused on examining the influence of support morphology, modifier loading, and their interactions on catalytic activity in the ECODS process.

2. Experimental

2.1. Materials

Tetraethyl orthosilicate (TEOS) (>99%), Pluronic P123, zirconium(IV) isopropoxide isopropanol complex (99.9%), zirconyl chloride octahydrate (98%), ammonium molybdate tetrahydrate (>99%), dibenzothiophene (98%), *n*-dodecane, pyridine (>99%), 2,5-hexanedione (>98%) and hydrogen peroxide (30%) were purchased from Sigma-Aldrich (St Louis, MO, USA). HCl (35%) was purchased from Stanlab (Lublin, Poland). 2-Propanol (>99%) was purchased from Chempur Poland.

2.2. Preparation of the long-channel SBA-15 support

The rod-like, long-channel mesoporous silica SBA-15 was synthesized *via* the hydrothermal method described in ref. 26. Initially, Pluronic P123 (poly(ethylene glycol)-*block*-poly(propylene glycol)-*block*-poly(ethylene glycol)) (16 g), a non-ionic surfactant, was dissolved in 600 mL of a 0.7 M HCl solution at 35 °C. To this mixture, tetraethyl orthosilicate (TEOS, 34.108 g), serving as the silica source, was added dropwise under continuous stirring. The resulting mixture was stirred at 35 °C for 20 hours, followed by hydrothermal treatment at 100 °C under static conditions for 24 hours in an oven. The white solid product was then filtered using a Büchner funnel, washed with 1200 mL of deionized water, and dried at room temperature. Finally, the surfactant template was removed by calcination at 500 °C for 8 hours at a heating rate of 1 °C min^{-1}. The sample was designated as SBA-15-L.

2.3. Preparation of the short-channel SBA-15 support

The synthesis of short-channel mesoporous silica SBA-15 was performed following the procedure outlined in ref. 7. Initially, Pluronic P123 (poly(ethylene glycol)-*block*-poly(propylene glycol)-*block*-poly(ethylene glycol)) (16 g) and $ZrOCl_2{\cdot}8H_2O$ (2.64 g) were dissolved in a mixture of distilled water (500 mL) and HCl (35%, 88 mL) at 35 °C with stirring for 22 hours. Subsequently, tetramethyl orthosilicate (TMOS, 24.798 g), used as the silica source, was added dropwise to the mixture under vigorous stirring. The resulting mixture was maintained at 35 °C for an additional 24 hours. Unlike other procedures, the zirconium species were not removed from the sample *via* sulfuric acid treatment. The solid white product was filtered using a Büchner funnel, washed with 1500 mL of distilled water, and dried at room temperature. Finally, the dried powder was calcined at 500 °C for 4 hours at a heating rate of 1 °C min^{-1}. The resulting sample was designated as ZrSBA-15-S.

2.4. Modification of SBA-15-L with zirconium species

Two grams of long-channel mesoporous silica SBA-15-L were dried overnight in an oven at 100 °C. The prepared sample was then transferred to a round-bottom flask and heated on a vacuum evaporator at 80 °C for 1 hour. Next, a suspension of zirconium(IV) isopropoxide isopropanol complex in water (20 mL of distilled water + 0.384 g of zirconium salt) was added dropwise to perform incipient wetness impregnation. The target Si/Zr molar ratio was 30. The mixture was then heated using a vacuum evaporator at 80 °C for 1 hour. The resulting white solid product was heated at 110 °C for 18 hours to enhance the degree of crystallization of zirconium oxide. Finally, the material was calcined at 500 °C for 4 hours with a temperature ramp of 3 °C min^{-1}. The final material was designated as Zr/SBA-15-L.

2.5. Modification of Zr/SBA-15-L and ZrSBA-15-S with molybdenum species

The obtained Zr/SBA-15-L and ZrSBA-15-S samples were then modified with molybdenum species using incipient wetness impregnation as follows. The target Si/Mo molar ratio was 30. To begin, 1 g of the sample, which had been dried overnight at 100 °C, was placed in a round-bottom flask. The sample was then heated on a vacuum evaporator at 80 °C for 1 hour. After this, an aqueous solution of molybdenum salt (0.098 g of ammonium molybdate tetrahydrate + 10 mL of distilled water) was added dropwise. The mixture was then heated on a vacuum evaporator at 80 °C until the distilled water was removed. The resulting solid white material was dried in an oven at 110 °C for 18 hours. Finally, the samples were calcined at 500 °C for 4 hours with a temperature ramp of 3 °C min^{-1}. The resulting samples were designated as Mo/Zr/SBA-15-L and Mo/ZrSBA-15-S.

2.6. Catalyst characterization

The prepared materials were analyzed by XRD measurements using a Bruker AXS D8 Advance diffractometer with Cu Kα radiation (λ = 0.154 nm). Data were collected in the low angle range of 2θ varied from 0.6° to 8° and in the wide angle range of 2θ from 6° to 60° with a resolution of 0.02° and 0.05°, respectively.

The surface area, pore volume, and diameter of the catalysts were determined by low-temperature N_2 adsorption/desorption measurements using a Micromeritics ASAP 2020 apparatus. Before analysis, the powder was outgassed at 300 °C for 8 h. The specific surface area values were determined using the Brunauer–Emmett–Teller (BET) method. The average pore diameter was determined using the density functional theory (DFT) method.

The structure of the produced catalysts was examined by field-emission scanning electron microscopy (FE-SEM) using a Quanta 250 FEG instrument (FEI, USA) at an accelerating voltage of 10 kV. Energy dispersive X-ray analysis (EDX) and EDX mapping were carried out using an EDS analyzer at a beam accelerating voltage of 30 kV. All measurements were performed on carbon adhesive conductive tape without metallization.

UV-vis spectra were recorded using a Varian-Cary 300 Scan UV-vis spectrophotometer with an integrated CA-30I sphere. The samples, first dried at 100 °C for 12 h, were placed in a cell equipped with a quartz window. The Kubelka–Munk function ($F(R)$) was used to convert reflectance measurements into equivalent absorption spectra. SPECTRALON was used as a reference sample.

XP spectra were recorded using an ultra-high-vacuum photoelectron spectrometer equipped with a Phoibos 150 NAP analyzer (SPECS, Germany). The operating pressure in the chamber was close to 5×10^{-9} mbar. The powders examined were irradiated with monochromatic Al Kα radiation (1486.6 eV). The binding energies of the obtained spectra were referenced to the C 1s peak at 284.6 eV.

Pyridine adsorption combined with FT-IR measurements was performed using a Bruker INVENIO S spectrometer equipped with an *in situ* vacuum cell. Prior to measurement, the catalysts were pressed into thin wafers and placed inside a homemade cell. The cell containing the sample was then outgassed at 350 °C for 2 hours. After this, pyridine was introduced at 150 °C. Once the sample was saturated with pyridine, the solid was degassed at 150 °C, 200 °C, 250 °C, and 300 °C under vacuum for 30 minutes at each temperature. The spectrum obtained after outgassing the sample at 350 °C for 2 hours (*i.e.*, without adsorbed pyridine) was subtracted from all recorded spectra. The number of Brønsted and Lewis acid sites was calculated using the Emeis extinction coefficients: for Brønsted acid sites (BAS), ε1550 = 1.67 μmol^{-1} cm and for Lewis acid sites (LAS), ε1440 = 2.22 μmol^{-1} cm.[27] The FT-IR-ATR (attenuated total reflectance) spectra of the powdered samples were obtained utilizing a Platinum ATR accessory on a Bruker Vertex 70 spectrometer.

2.7. Catalytic tests

2.7.1. Cyclization and dehydration of 2,5-hexanedione. The catalysts were tested in the dehydration and cyclization of 2,5-hexanedione (2,5-HDN) as a probe reaction. The transformation was carried out in a tubular downflow reactor (∅: 8 mm; length: 80 mm) at atmospheric pressure, using nitrogen as the carrier gas. The granulated catalyst bed (0.5 < ∅ < 1.0 mm) (0.05 g) was initially heated at 350 °C for 2 hours under a nitrogen flow (40 mL min^{-1}) to remove any moisture present in the pores of the sample. Subsequently, 0.5 mL of 2,5-hexanedione was continuously passed through the catalyst at 350 °C. The substrate was delivered *via* a pump system (KD Scientific) and vaporized before entering the catalyst bed, with nitrogen acting as the carrier gas (40 mL min^{-1}). The reaction products were collected for 30 minutes in a cold trap (a mixture of liquid nitrogen and 2-propanol) and analyzed by gas chromatography (SRI 310 C, MXT-1 column, 30 m, column temperature: 100 °C) using a thermal conductivity detector (TCD). Helium was used as the carrier gas.

2.7.2. Dehydration and dehydrogenation of 2-propanol. The dehydration and dehydrogenation of 2-propanol were per-

formed using a microcatalytic pulse reactor (∅: 6 mm; length: 80 mm) inserted between the sample input and the column of an SRI 310 chromatograph. A 0.02 g portion of the granulated catalyst (0.5 < ∅ < 1.0 mm) was activated at 350 °C (heating rate 10 °C min^{-1}) for 2 hours under a nitrogen flow (40 mL min^{-1}). The 2-propanol conversion was analyzed over the temperature range of 150–300 °C using 3 μL pulses of alcohol under a nitrogen flow (65 mL min^{-1}) as the carrier gas. The substrate was vaporized before being passed through the catalyst bed with the nitrogen carrier gas. The reaction mixture was separated on a 2 m column filled with Carbowax 400 loaded on Chromosorb W (80–100 mesh) at 65 °C under a nitrogen flow (40 mL min^{-1}) and detected using a flame ionization detector (FID).

2.7.3. Extractive catalytic oxidative desulfurization (ECODS). The extractive catalytic oxidative desulfurization (ECODS) of dibenzothiophene (DBT) was performed in a glass reactor using an EasyMax Workstation. The ECODS studies were carried out using the following mixture: 500 ppm DBT in *n*-dodecane (5 mL), acetonitrile (5 mL), 0.5 wt% catalyst, and hydrogen peroxide (30%; H_2O_2/DBT = 6, 4, or 2). Prior to the reaction, the catalysts were heated at 400 °C for 8 hours to remove moisture from their pores. The dried catalysts were then placed into a test tube of the EasyMax Workstation. A suitable amount of DBT in *n*-dodecane, along with acetonitrile, was added. Once the reaction mixture reached the desired temperature, hydrogen peroxide was added dropwise. The reaction was conducted for 120 minutes at 60 °C. The removal of DBT was monitored from the oil phase, with samples of the reactants taken at regular time intervals. The conversion of DBT was calculated using the following equation:

$$\%\ \text{Conversion of DBT} = \frac{(C_0 - C)}{C_0} \times 100\% \quad (1)$$

where C_0 is the concentration of DBT at the beginning of the reaction and C is the concentration of DBT during the progress of the reaction.

A gas chromatograph (GC, Thermo Scientific, Trace 1300) equipped with a 30 m DB-1 column and an FID detector was used to determine the concentration of DBT during the reaction process. Helium was used as the carrier gas. The injector and detector temperatures were set to 250 °C and 280 °C, respectively. The column's initial temperature was set to 80 °C for 3 minutes, after which it was increased to 300 °C with a temperature ramp of 10 °C min^{-1}.

After the first reaction run, the samples were separated from the reaction mixture using a Büchner funnel, washed with acetonitrile (3 portions of 10 mL each), and dried at 100 °C for 12 hours. The dried samples were then heated to 400 °C for 8 hours before being used in the next reaction run.

3. Results and discussion

The texture and structural properties of the synthesized catalysts were evaluated using low-temperature nitrogen adsorption/desorption isotherms and X-ray diffraction measurements. Additionally, the morphology of ZrSBA-15-S was examined using scanning electron microscopy images.

The N_2 adsorption/desorption isotherms of long-channel SBA-15-L and short-channel ZrSBA-15-S, as shown in Fig. 1, can be classified as type IV(a) according to the IUPAC classification, confirming the mesoporous nature of both silica supports.[28,29] The hysteresis loop in the N_2 adsorption/desorption isotherms of long-channel SBA-15-L is of type H1, whereas the isotherms of short-channel ZrSBA-15-S display hysteresis loops of type H2(b). Additionally, ZrSBA-15-S shows a lower amount of nitrogen adsorption. These differences between the two silica supports can be attributed to their distinct morphologies: the plate-like structure of ZrSBA-15-S compared to the rod-like morphology of SBA-15-L.

Both silica supports, SBA-15-L and ZrSBA-15-S, exhibit relatively large surface areas of 926 and 753 $m^2\ g^{-1}$, respectively, along with some microporosity, which is more pronounced in the short-channel ZrSBA-15-S (Table 1). The formation of micropores in the silica skeletons of both materials is attributed to the use of Pluronic P123 as a surfactant, followed by its removal during calcination.[30] Long-channel SBA-15-L shows almost twice the mesopore volume compared to that of ZrSBA-15-S, due to the formation of rod-like channels that serve as mesopores. In contrast, ZrSBA-15-S has a higher wall diameter, which leads to a reduction in its pore diameter. This difference is a result of the incorporation of zirconium species into the silica framework, which increases the wall thickness. Modification of both SBA-15 supports with metal precursors (Zr or Mo) results in a decrease in total surface area, as well as in the areas and volumes of micropores and mesopores, alongside a reduction in pore diameter. These changes are accompanied by an increase in wall thickness. The observed differences in structural parameters after metal incorporation may be due to the partial coverage of the pores of SBA-15-L and ZrSBA-15-S by the metal modifiers or the introduction of metal species into the silica skeleton. Additionally, the modification of both supports with metal precursors leads to a decrease in the unit cell parameter (a_0) and the interplanar spacing (d_{100}), causing a contraction of the hexagonal structure

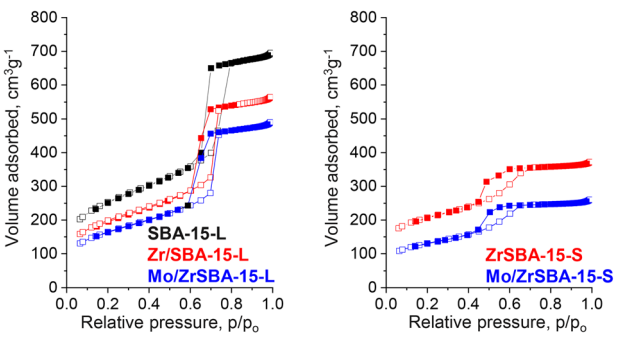

Fig. 1 Nitrogen adsorption/desorption isotherms of the SBA-15 based samples.

Table 1 Textural/structural parameters and chemical composition of the obtained samples

Catalyst	S, $m^2\ g^{-1}$	S_{micro}, $m^2\ g^{-1}$	$V_{mesop.}$, $cm^3\ g^{-1}$	$V_{microp.}$, $cm^3\ g^{-1}$	d, nm	d_{wall} [a], nm	a_0 [a], nm	d_{100} [a], nm	Molar ratio based on XPS	
									Si/Zr	Si/Mo
SBA-15-L	926	222	1.00	0.08	11.7	1.85	9.39	8.13	—	—
Zr/SBA-15-L	725	161	0.83	0.06	9.6	2.09	9.00	7.80	36	—
Mo/Zr/SBA-15-L	599	93	0.72	0.03	9.6	2.13	8.48	7.34	53	146
ZrSBA-15-S	753	338	0.55	0.14	6.7	3.32	8.48	7.34	25	—
Mo/ZrSBA-15-S	475	144	0.37	0.06	6.6	3.60	8.17	7.08	24	58
Mo/ZrSBA-15-S reused	—	—	—	—	—	—	—	—	25	304

[a] Calculated from XRD; S – specific surface area determined by the BET method; V – pore volume; d – pore diameter; d_{wall} – wall thickness; a_0 – unit cell parameter; d_{100} – inter-space distance.

of the SBA-15 materials due to the additional thermal treatment after modifier loading.

The low-angle XRD patterns of the synthesized catalysts, as shown in Fig. 2, exhibit reflexes characteristic of the hexagonal structure of SBA-15. The most prominent reflex at approximately 1° 2θ ([100]), according to the literature, is attributed to the regular interspace distances between the silica walls of the mesoporous channels. The other two peaks at around 1.5° and 1.7° 2θ ([110] and [200], respectively), correspond to the long-range ordering of the silica framework.[31,32] The absence of the peak at around 1.7° 2θ in the XRD pattern of ZrSBA-15-S may be due to the differing structural morphology of this material, which does not display the typical rod-like channels of SBA-15. Interestingly, the wide-angle XRD patterns of the molybdenum- and zirconium-containing samples do not show diffraction peaks typically associated with crystalline molybdenum or zirconium oxides. The lack of these reflexes suggests that the crystals of these oxides on the surface of the mesoporous silica supports may be too small to be detected by XRD or may have an amorphous character. For all the analyzed samples, only a broad reflex in the range of 15–35° 2θ is observed, which, according to the literature, is indicative of the amorphous nature of the samples.[6]

The SEM images shown in Fig. 3 confirm the successful synthesis of short-channel Mo/ZrSBA-15-S and long-channel Mo/Zr/SBA-15-L. The image of Mo/ZrSBA-15-S reveals the characteristic cross-disc-like particles typical of short-channel SBA-15,[7,31] whereas in the case of Mo/Zr/SBA-15-L, longer rods are observed. Notably, the images of both materials show no extra particles, consistent with the wide-angle XRD patterns, which indicated the absence of metal oxide crystals on the surface of the catalysts.

The distribution of Mo and Zr species on the surface of both silicas was evaluated using SEM-EDS. As shown in the elemental mapping presented in Fig. 4, all species are uniformly dispersed across the Mo/Zr/SBA-15-L and Mo/ZrSBA-15-S surfaces.

The coordination of zirconium and molybdenum species on the surface of the synthesized catalysts was evaluated using the UV-vis spectra shown in Fig. 5. A low-intensity band at around 200 nm, associated with defects in the silica, is detected in the spectra of all samples.[33] For the samples containing zirconium species, the UV-vis spectra show an increase in absorption compared to that of SBA-15-L with the appearance of low-intensity bands between 220 and 350 nm. These bands are likely due to charge transfer between oxygen and zirconium in ZrO_2, or they may indicate the presence of multi-coordinated zirconium species with varying coordination numbers, or bands corresponding to zirconium dioxide oligomers, dimers, and trimers involving Zr–O–Zr bonding.[7,34] It is noteworthy that the increase in the absorption line is more pronounced in the UV-vis spectrum of Zr/SBA-15-L compared to that of ZrSBA-15-S, despite the latter having a higher zirconium content, as shown in Table 1. This observation suggests

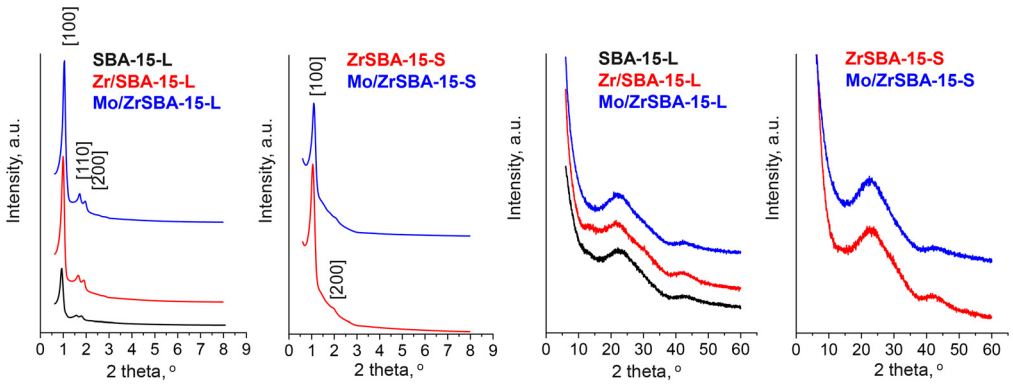

Fig. 2 Low- and wide-angle XRD patterns of the synthesized catalysts.

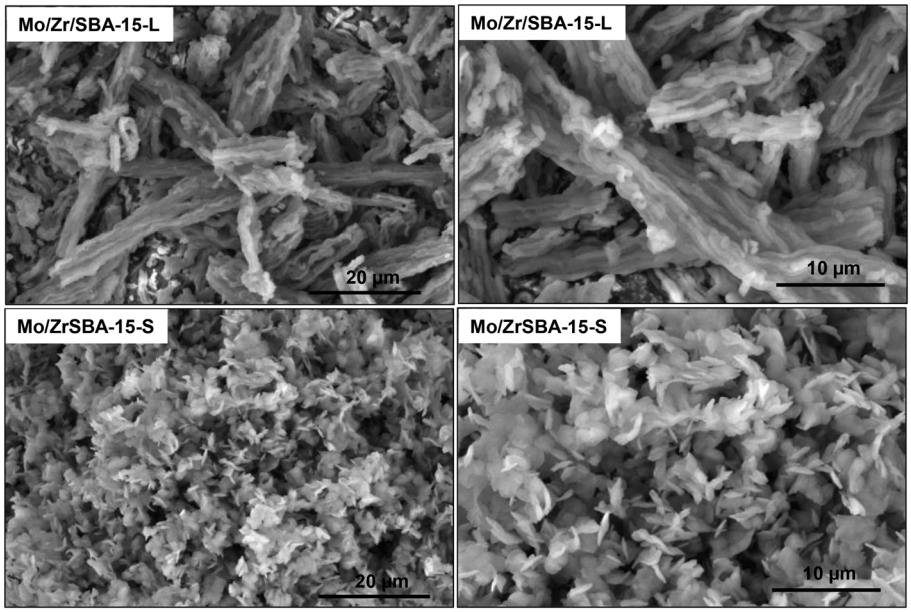

Fig. 3 SEM images of the Mo/Zr/SBA-15-L and Mo/ZrSBA-15-S samples.

that in ZrSBA-15-S, the zirconium species are predominantly incorporated into the silica skeleton, with only a small portion forming ZrO_2 on the surface. In contrast, the more noticeable increase in absorption in the UV-vis spectrum of Zr/SBA-15-L suggests that a higher concentration of ZrO_2 is present on the surface of this material in extra-framework positions.

Modification of the zirconium-containing samples with molybdenum species results in the appearance of a new broad band with a maximum at approximately 232 nm in the UV-vis spectra of Mo/Zr/SBA-15-L and Mo/ZrSBA-15-S. Deconvolution of this band reveals two distinct regions: 215–230 nm and 270–280 nm. These bands can be attributed to electron transfer between oxygen and molybdenum in tetrahedral coordination and the characteristic band of Mo–O–Mo oligomers, respectively.[5,35] Notably, the intensities of these bands, related to the different forms of molybdenum species, are similar in Mo/Zr/SBA-15-L. In contrast, for Mo/ZrSBA-15-S, the band corresponding to tetrahedrally coordinated molybdenum is more intense. This suggests that molybdenum species are more effectively incorporated into the ZrSBA-15-S support than the Zr/SBA-15-L support.

FT-IR-ATR spectroscopy confirmed the presence of molybdenum species on the surfaces of Mo/Zr/SBA-15-L and Mo/ZrSBA-15-S. Fig. 6 illustrates that the spectra of all samples exhibit bands at 456 cm^{-1}, 804 cm^{-1}, and 1074/1080 cm^{-1}, which correspond to the bending vibration of SiO_4 and the symmetric and asymmetric stretching vibrations of Si–O–Si. Following the introduction of molybdenum species, additional bands appear in the spectra at 562 cm^{-1}, 905/914 cm^{-1}, and 954/962 cm^{-1}. The initial two bands are associated with the stretching mode of oxygen connected to the molybdenum atoms in Mo–O–Mo, while the latter band pertains to the vibration of the bond in Mo=O species.[36,37]

The states of zirconium and molybdenum species were further investigated using X-ray photoelectron (XP) spectra, as shown in Fig. 7. The doublet in the Zr 3d region, corresponding to Zr $3d_{3/2}$ and Zr $3d_{5/2}$ at binding energies (BE) of 185.8–184.8 eV and 183.6–183.1 eV, respectively, confirms the presence of Zr^{4+}.[38,39] Data from the literature indicate that the BE of the Zr $3d_{5/2}$ band in ZrO_2 is typically 182.5 eV.[38] For both Zr/SBA-15-L and ZrSBA-15-S, the BE of the Zr $3d_{5/2}$ band is higher than that observed for pure ZrO_2. In Zr/SBA-15-L, the BE is closer to the value typical of ZrO_2, suggesting the presence of zirconium(IV) oxide on the surface. In contrast, the Zr $3d_{5/2}$ band in ZrSBA-15-S is shifted to a higher BE, indicating the incorporation of zirconium into the silica framework and the formation of Zr–O–Si species. This is consistent with the observed increase in wall thickness in ZrSBA-15-S, further supporting the idea that zirconium species are embedded in the silica structure. These differences in the position of the Zr $3d_{5/2}$ band imply a stronger interaction between zirconium species and the silica skeleton in ZrSBA-15-S compared to that in Zr/SBA-15-L. Additionally, the intensity of the Zr $3d_{5/2}$ band is higher in ZrSBA-15-S, reflecting the greater zirconium loading in this sample. The presence of zirconium species in both ZrSBA-15-S and Zr/SBA-15-L also induces changes in the O 1s region of the XP spectra. For both short- and long-channel silicas, two bands are observed at 532.9 eV and 531.9–531.5 eV. The first band, at 532.9 eV, is characteristic of Si–O–Si, while the second band can be assigned to Si–O–Zr or Zr–OH.[38,39] The shift in the position of the second band between ZrSBA-15-S and Zr/SBA-15-L suggests that, in ZrSBA-15-S, this band corresponds to Si–O–Zr, confirming the incorporation of zirconium into the silica framework. In contrast, in Zr/SBA-15-L, the band likely corresponds to Zr–OH species in the hydrated ZrO_2 particles on the silica surface.

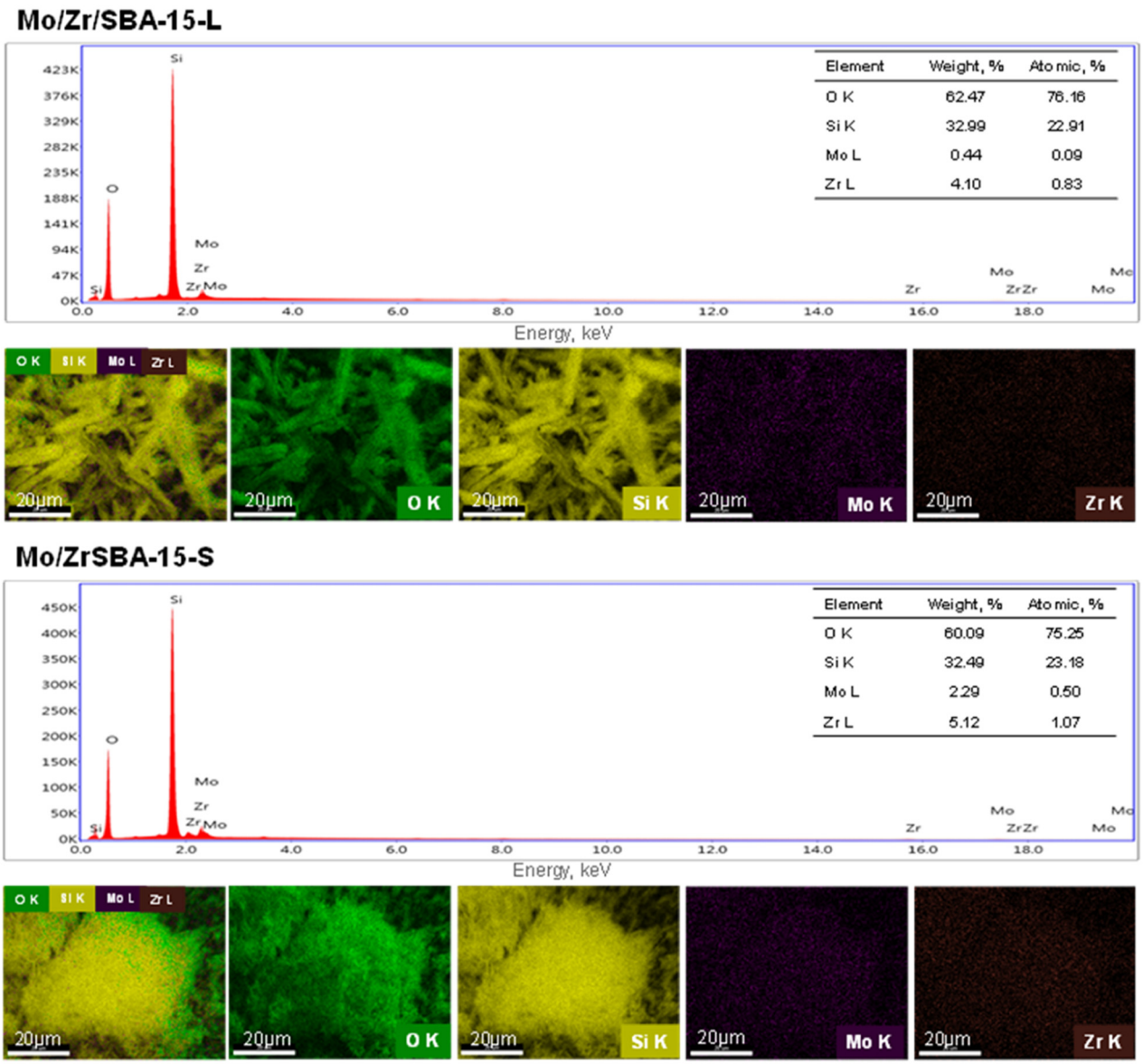

Fig. 4 EDS elemental mapping images of the silica-based materials and the weight and atomic percentages of the elements in Mo/Zr/SBA-15-L and Mo/ZrSBA-15-S.

Notably, the BE of the second band is higher in ZrSBA-15-S, further indicating a stronger interaction between zirconium species and the silica framework in this material, which aligns with the findings from the Zr 3d region.

The modification of ZrSBA-15-S and Zr/SBA-15-L with molybdenum species leads to changes in the Si 2p, O 1s, and Zr 3d regions in the XP spectra of Mo/ZrSBA-15-S and Mo/Zr/SBA-15-L, along with the appearance of new bands in the Mo 3d region. A doublet in the Mo 3d region, corresponding to Mo $3d_{3/2}$ and Mo $3d_{5/2}$ at approximately 235 eV and 232.2–231.7 eV, respectively, confirms the presence of Mo^{6+} species linked by oxygen atoms to the silica surface.[40,41] Notably, the introduction of molybdenum onto the silica surface results in a shift of the binding energies (BE) of the Si 2p, O 1s, and Zr 3d bands to lower values in the XP spectrum of Mo/ZrSBA-15-S and to higher values in the spectrum of Mo/Zr/SBA-15-L. This suggests that electrons are transferred from the molybdenum species to the ZrSBA-15-S support, while the reverse occurs for Mo/Zr/SBA-15-L, where electron mobility from the Zr/SBA-15-L support to the molybdenum species is observed. Additionally, the BE of the Mo 3d bands is higher in Mo/ZrSBA-15-S compared to that in Mo/Zr/SBA-15-L. According to the literature, the strength of the molybdenum–support interaction is reflected in the BE of the Mo 3d bands: the stronger the interaction, the higher the binding energy of the bands.[40] Therefore, the observed differences in the BE of the Mo 3d bands in the spectra of Mo/ZrSBA-15-S and Mo/Zr/SBA-15-L suggest that the interaction between molybdenum

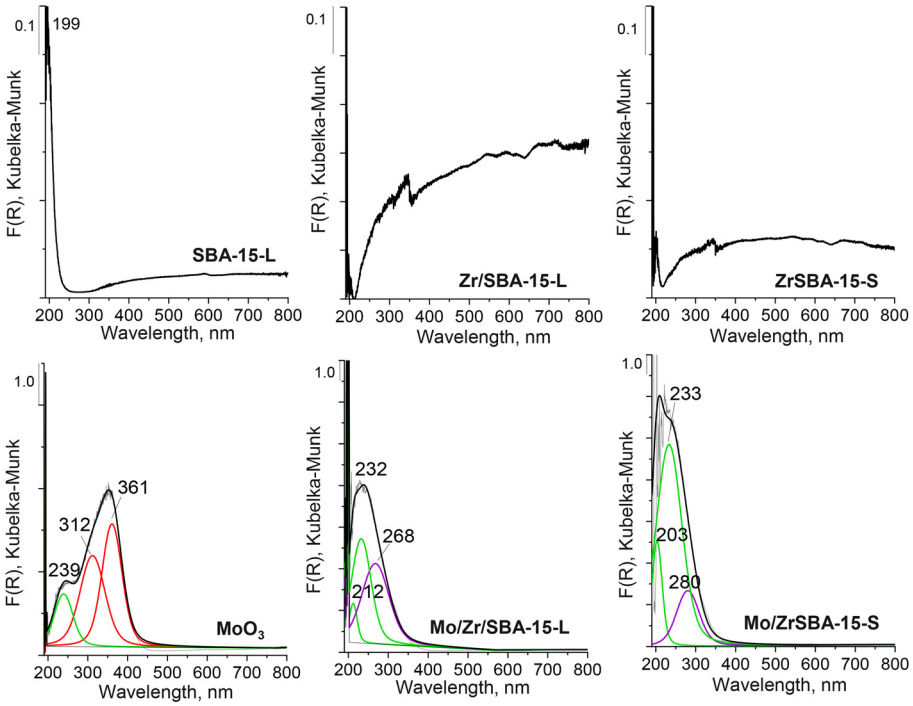

Fig. 5 UV-vis spectra of SBA-15-L, MoO_3 and modified silicas.

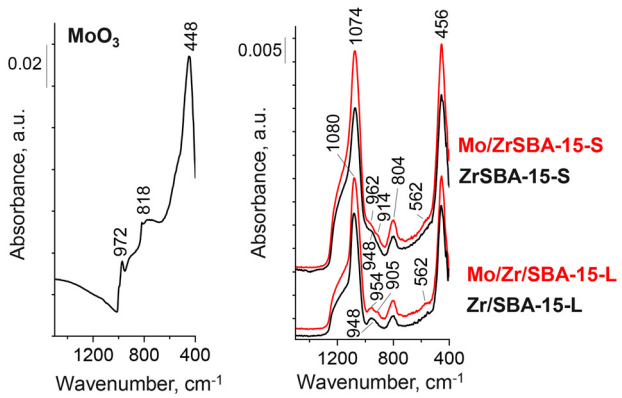

Fig. 6 FT-IR-ATR spectra of the MoO_3- and SBA-15-based synthesized samples.

species and the short-channel SBA-15 support is stronger than that with the long-channel SBA-15 support.

The differences observed in the XP spectra could also be attributed to the varying loading of zirconium and molybdenum species in the prepared samples, as summarized in Table 1. The Si/Zr molar ratios for ZrSBA-15-S and Zr/SBA-15-L are 25 and 36, respectively. After the loading of molybdenum species, these ratios change to 24 for Mo/ZrSBA-15-S and 53 for Mo/Zr/SBA-15-L. This suggests that the zirconium species loaded onto the SBA-15-L surface are not strongly bonded to the silica, and they may be leached during the modification process with molybdenum species through wetness impregnation. Furthermore, the Si/Mo molar ratio is more distinct, standing at 58 for short-channel silica (ZrSBA-15-S) and 146 for long-channel silica (Zr/SBA-15-L). The higher amount of molybdenum loaded on the surface of Mo/ZrSBA-15-S is likely due to the stronger interaction between the support and the molybdenum species, which results in more efficient loading of the modifier.

The estimation of the number and strength of acid sites was performed by pyridine adsorption combined with FT-IR measurements. This method is based on the interaction of pyridine with Lewis or Brønsted acid sites, resulting in characteristic bands in the FT-IR spectra. The bands corresponding to pyridine coordinated to Lewis acid sites (LAS) appear at approximately 1610 cm^{-1} and 1449 cm^{-1}. Bands indicative of pyridine protonation at Brønsted acid sites (BAS), which lead to the formation of pyridine cations, are observed at around 1639 cm^{-1} and 1545 cm^{-1}. Additionally, a band at around 1490 cm^{-1} typically results from the interaction of pyridine with both Lewis and Brønsted acid sites. Other bands may also appear in the FT-IR spectrum following pyridine adsorption, including those due to hydrogen-bonded pyridine at approximately 1598 cm^{-1} and 1447 cm^{-1}, as well as a band at around 1578 cm^{-1}, which is characteristic of physiosorbed pyridine.[27,42–44]

The FT-IR spectrum of Zr/SBA-15-L, as shown in Fig. 8, reveals only bands associated with hydrogen-bonded pyridine. This suggests that the zirconium species are not incorporated into the silica skeleton of this material, but are most likely present as amorphous ZrO_2 particles on the silica surface. These zirconium species interact with pyridine through Zr–OH groups, acting as weak Brønsted acid sites (BAS), along with

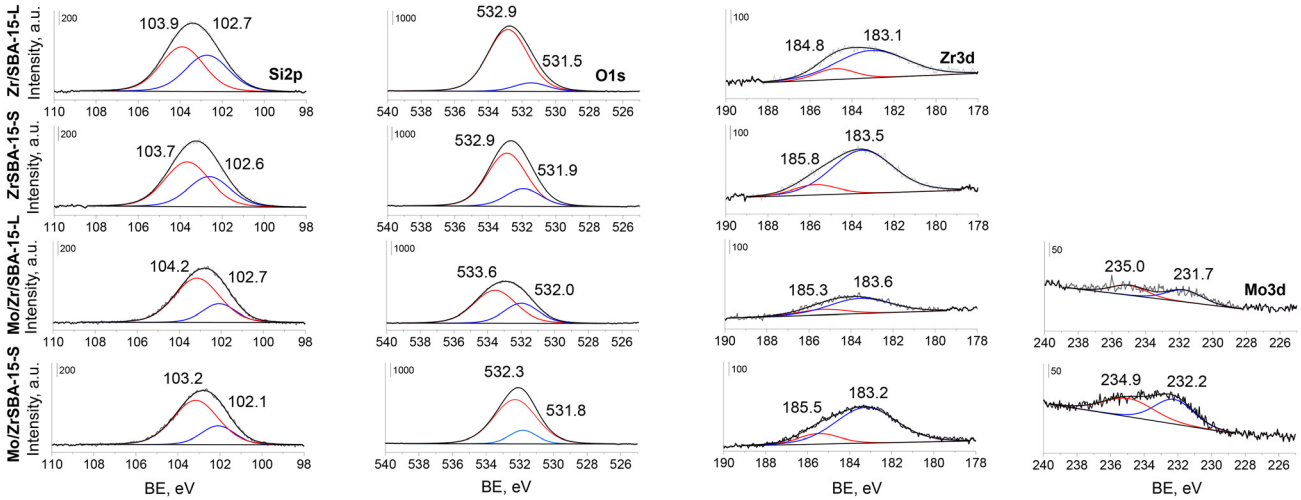

Fig. 7 XP spectra of the Si 2p, O 1s, Zr 3d and Mo 3d regions.

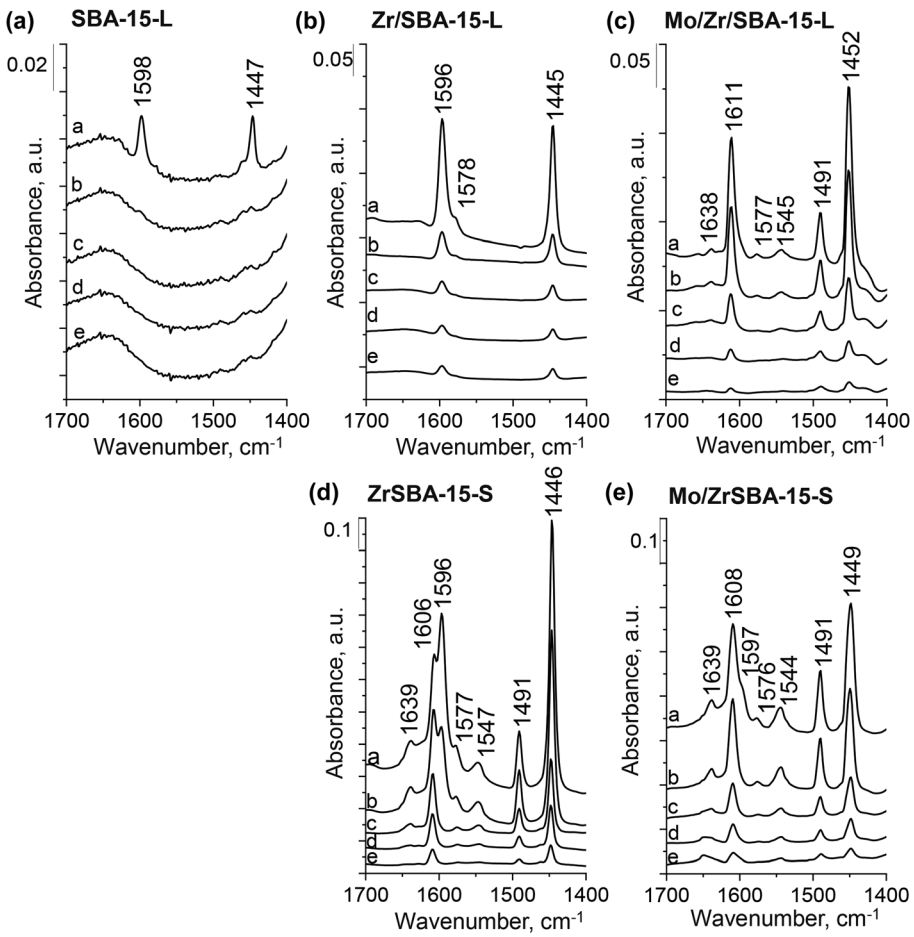

Fig. 8 FT-IR spectra of the materials after pyridine adsorption and evacuation for 5 min at 150 °C (a) and after evacuation for 30 min at 150 °C (b), 200 °C (c), 250 °C (d), and 300 °C (e). Spectra were normalized to 10 mg of the samples. The spectra of the activated samples under vacuum were subtracted from all spectra recorded after pyridine adsorption and evacuation.

the silanol species of the silica. Comparing the spectra of SBA-15-L and Zr/SBA-15-L, it is evident that pyridine forms only weak hydrogen bonds with the silanols in SBA-15-L (the bands at 1598 cm^{-1} and 1447 cm^{-1} disappear after evacuation at 150 °C). However, in Zr/SBA-15-L, pyridine is more strongly hydrogen-bonded to the Zr–OH species, as these FT-IR bands

remain even after evacuation at 300 °C. The FT-IR spectra of ZrSBA-15-S show distinct features. Similar to Zr/SBA-15-L, bands corresponding to pyridine hydrogen-bonded to weak BAS are observed (the bands at 1446 cm^{-1} overlap with the band from pyridine coordinated to Lewis acid sites (LAS) and the band at 1596 cm^{-1}). The band at 1596 cm^{-1} disappears after evacuation at 200 °C, suggesting that it is primarily due to pyridine hydrogen-bonded to silanols. Additionally, new bands at 1547 cm^{-1} and 1639 cm^{-1}, characteristic of pyridine cations resulting from interaction with strong BAS, confirm that zirconium species have been incorporated into the silica skeleton during synthesis, forming Zr–O(H)–Si bridges. According to the literature, these Zr–O(H)–Si bridges act as strong BAS.[45,46] The FT-IR spectrum of ZrSBA-15-S also shows bands from pyridine adsorbed on LAS (1446 cm^{-1} and 1606 cm^{-1}), which remain stable up to 300 °C under vacuum outgassing.

The loading of molybdenum species onto zirconium-containing samples induces differences in the acidic properties of the obtained catalysts. Modification of Zr/SBA-15-L with molybdenum results in the formation of both Lewis and Brønsted acid sites, as confirmed by pairs of FT-IR bands at 1452 cm^{-1} and 1611 cm^{-1} (associated with Lewis acid sites, LAS) and at 1545 cm^{-1} and 1638 cm^{-1} (corresponding to Brønsted acid sites, BAS). The bands assigned to pyridine chemisorbed on LAS persist even after evacuation at 300 °C, indicating the presence of relatively stable Lewis acidic sites. However, Zr/SBA-15-L does not exhibit strong acidic sites, suggesting that the formation of strong BAS and LAS in Mo/Zr/SBA-15-L is likely due to the incorporation of molybdenum species onto this support. The literature suggests that the formation of BAS on silica modified with molybdenum species is driven by the interaction between silanol groups and adjacent surface molybdate species, leading to the formation of pseudo-bridging Si–O(H)···Mo(=O)$_2$ species. Additionally, LAS formation could be attributed to the presence of coordinatively unsaturated molybdenum centers.[47,48] In the case of Mo/ZrSBA-15-S, modification with molybdenum species results in a decrease in the number of LAS and weak BAS, while the number of strong BAS increases, as shown in Table 2. Notably, the strength of BAS protonating pyridinium and coordinatively unsaturated LAS in Mo/ZrSBA-15-S is higher than that in Mo/Zr/SBA-15-L, as evidenced by the more intense FT-IR bands characteristic of pyridinium cations (BAS) and coordinatively bonded pyridine (LAS), which remain stable even after evacuation at 300 °C in the former sample. The changes in the number of LAS and BAS in Mo/ZrSBA-15-S compared to that in ZrSBA-15-S, as illustrated in Table 2, are likely due to the partial coverage of surface LAS and BAS on ZrSBA-15-S by the molybdenum species. The increase in the strength of both LAS and BAS may result from interactions between the bridged hydroxyl groups associated with zirconium species (acting as BAS) and adjacent surface molybdenum species, as depicted in Scheme 1. Furthermore, Mo/ZrSBA-15-S possesses a higher number of LAS and BAS than Mo/Zr/SBA-15-L, likely due to the greater amount of molybdenum and zirconium species loaded onto the support, which are the primary sources of acidity.

The FT-IR spectra in the hydroxyl stretching region of the samples activated at 350 °C for 2 hours under vacuum are presented in Fig. 9. The most intense, sharp band at around 3740 cm^{-1} in the Zr-containing samples corresponds to the O–H stretching vibration of free hydroxyl groups, which are found in both the silica SBA-15 (silanol groups) and zirconia

Table 2 Number of Lewis (based on the band at *ca.*1450 cm^{-1}) and strong Brønsted (based on the band at *ca.* 1545 cm^{-1}) acid sites calculated from pyridine adsorption[a]

	Lewis acid sites, μmol g^{-1}			Brønsted acid sites, μmol g^{-1}				
Catalyst	200 °C	250 °C	300 °C	150 °C[b]	150 °C	200 °C	250 °C	300 °C
Zr/SBA-15-L	—	—	—	—	—	—	—	—
Mo/Zr/SBA-15-L	23	9	5	11	7	4	1	1
ZrSBA-15-S	139	84	39	58	54	24	9	3
Mo/ZrSBA-15-S	47	28	13	46	43	16	10	6

[a] BAS extinction coefficient, ε_{1550} = 1.67 μmol^{-1} cm; LAS extinction coefficient, ε_{1440} = 2.22 μmol^{-1} cm. [b] Evacuation for 5 min.

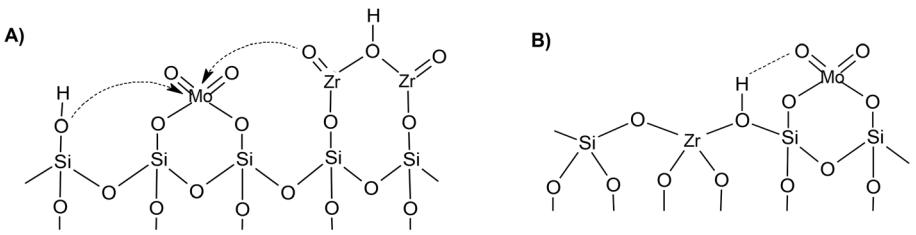

Scheme 1 Possible interactions between the Si–O(H)–Si and ZrO_2 dimers with pseudo-bridging Si–O(H)···Mo(=O)$_2$ species on the Mo/Zr/SBA-15-L surface (A) and with pseudo-bridging Zr–O(H)···Mo(=O)$_2$ species on the Mo/ZrSBA-15-S surface (B).

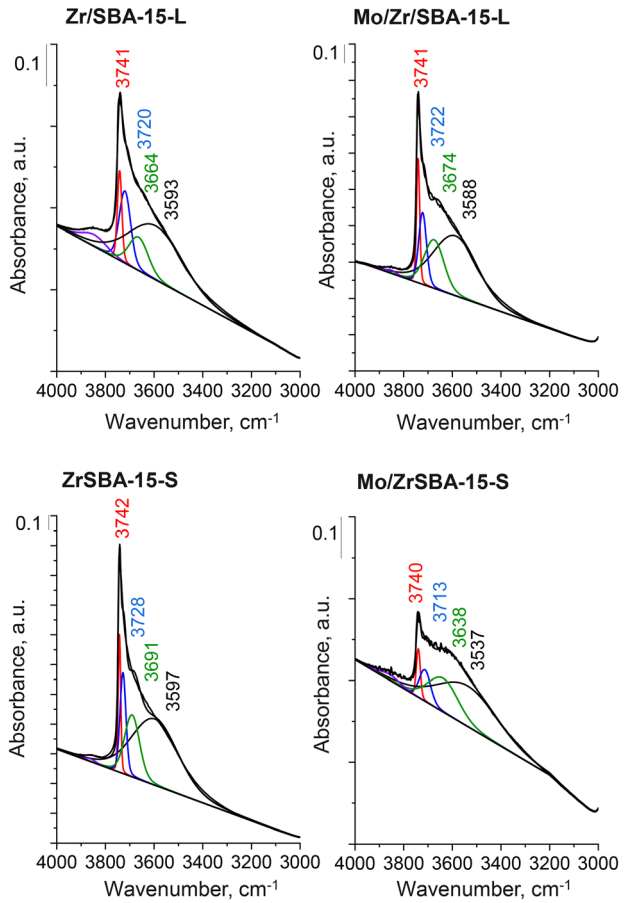

Fig. 9 FT-IR spectra in the stretching hydroxyl region of the samples activated at 350 °C for 2 h under vacuum. Spectra were normalized to 10 mg of the samples.

species (Zr–OH, *i.e.*, hydroxyls of type I, where one OH group is attached to a single surface site).[49] This band is accompanied by a broad tail that covers various types of hydroxyl groups. Deconvolution of the band reveals additional hydroxyl species. However, the unambiguous assignment of these bands is challenging, as the crystal structure of the zirconium oxide species is not fully known in this study. The band at approximately 3720 (3728) cm^{-1} is attributed to double-bridged hydroxyl groups.[49–53] Hoffmann and Knozinger[54] proposed that pairs of bands at 3715 and 3510 cm^{-1} correspond to hydrogen-bonded vicinal silanols, which in our spectra appear as bands at 3720/3728 cm^{-1} and 3593/3597 cm^{-1}, respectively. Interestingly, the positions of these bands are similar for both Zr/SBA-15-L and ZrSBA-15-S. However, the bands at 3664 cm^{-1} for Zr/SBA-15-L and at 3691 cm^{-1} for ZrSBA-15-S differ by 27 cm^{-1}, suggesting the presence of different OH species. This band is generally assigned to type II (where one OH group is attached to two surface sites) or type III (where one OH group is attached to three surface sites).[49] Based on this, it can be proposed that in Zr/SBA-15-L, the band at 3664 cm^{-1} corresponds to the bridged hydroxyls between two Zr atoms (Zr–O(H)–Zr), whereas in ZrSBA-15-S, the band at 3691 cm^{-1} originates from the stretching vibrations of Zr–O(H)–Si bridged hydroxyls. This interpretation is consistent with the results from XPS and the increased wall thickness calculated from XRD for ZrSBA-15-S, suggesting the incorporation of zirconium into the silica skeleton.

The modification of Zr-containing supports with molybdenum precursor induces only slight changes in the position of the bridged hydroxyl band in Mo/Zr/SBA-15-L (shifting from 3664 cm^{-1} to 3674 cm^{-1}). In contrast, for Mo/ZrSBA-15-S, the shift is more pronounced, with the band moving from 3691 cm^{-1} to 3638 cm^{-1}, reflecting an increase in the acidity strength of the OH groups, as confirmed by the pyridine adsorption results. The shift towards a lower wavelength is indicative of stronger acidic sites, which suggests that molybdenum species interact more effectively with the zirconium-modified silica. A significant shift is also observed in the broad band associated with hydrogen-bonded hydroxyls, moving from 3597 cm^{-1} to 3537 cm^{-1} in Mo/ZrSBA-15-S. This indicates a strong interaction between the bridged Zr–O(H)–Si groups and the molybdenum species. Based on these shifts, along with the XPS data and pyridine adsorption measurements, it can be concluded that there is a strong interaction between the bridged Zr–O(H)–Si hydroxyl groups and the molybdenum species, as illustrated in Scheme 1.

The comparative analysis of the FT-IR bands in the hydroxyl region before and after the introduction of molybdenum species reveals significant differences between the short- and long-channel materials (Fig. 10). For the ZrSBA-15-S sample, a significant decrease in the intensity of the FT-IR bands associated with all types of hydroxyls on the surface is observed after the introduction of molybdenum species. This suggests a strong interaction between the molybdenum species and the surface hydroxyl groups of the support, likely due to the interaction between the zirconium-modified silica and the molybdenum species, which alters the hydroxyl environment. In contrast, for the long-channel material (Zr/SBA-15-L), the opposite phenomenon occurs. After the introduction of molybdenum species, the intensity of the bands in the hydroxyl region significantly increases. This suggests that zirconium introduced

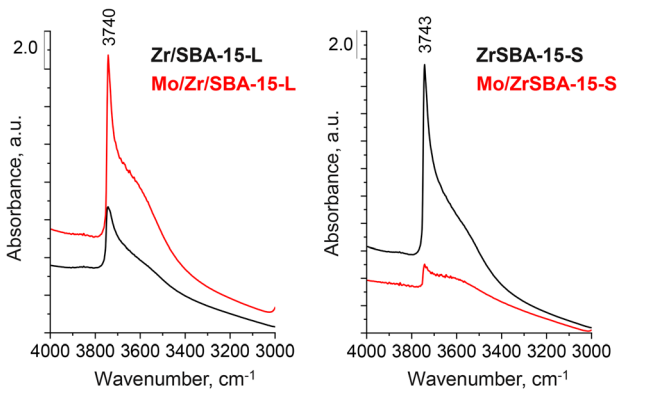

Fig. 10 FT-IR spectra of the hydroxyl region before and after the introduction of molybdenum species into the zirconium-containing samples. Spectra were normalized to 10 mg of the samples.

into SBA-15-L by impregnation interacts with the silica surface through silanols. However, the impregnation with the molybdenum precursor causes some zirconium species to leach off (as indicated in Table 1), revealing more surface silanols. The increase in the number of free silanols allows for the formation of pseudo-bridged silanol groups with the molybdenum species,[47] which exhibit lower acidity compared to the zirconium hydroxyl species (Zr–OH). This interaction leads to a shift in the OH region of the FT-IR spectrum from 3664 cm^{-1} to 3674 cm^{-1}, reflecting the altered nature of the hydroxyl groups after molybdenum modification.

The acid–base properties of the samples were further evaluated by performing test reactions, specifically the dehydration and dehydrogenation of 2-propanol. In these reactions, the formation of propene and diisopropyl ether indicates the involvement of acid sites (or acid–base pairs), while the formation of acetone requires the presence of basic or redox sites on the catalyst surface.[55] The results of these reactions are presented in Fig. 11. The modification of long-channel SBA-15 (Zr/SBA-15-L) with zirconium species leads to the generation of both basic sites and acid–base pairs, as evidenced by the formation of acetone and diisopropyl ether, respectively. However, despite this, the conversion of 2-propanol (2-PrOH) on Zr/SBA-15-L remains low, reaching only 8% at 300 °C, which is comparable to the conversion observed on pristine SBA-15-L (10% at 300 °C). The formation of acetone suggests the presence of strong basic sites on the surface of Zr/SBA-15-L. According to data in the literature,[45,56] ZrO_2 particles loaded onto the silica surface contribute to the basicity, due to the basic oxygen species present on ZrO_2. These results align with those of the XPS analysis, which showed the formation of ZrO_2 particles on the surface of Zr/SBA-15-L, confirming the basicity observed in the test reactions.

The activity of ZrSBA-15-S in the 2-propanol dehydration and dehydrogenation reaction is significantly higher than that of Zr/SBA-15-L. ZrSBA-15-S achieves a 63% substrate conversion at 300 °C, with the selectivity toward propene and diisopropyl ether. These products indicate the presence of both basic and acidic sites on the surface of ZrSBA-15-S. However, the basic sites are not as strong as those observed on Zr/SBA-15-L, as evidenced by the absence of acetone formation in the reaction.[55] This suggests that the zirconium species in ZrSBA-15-S are not present in as high a concentration as amorphous ZrO_2 particles, as observed in Zr/SBA-15-L. Instead, zirconium is more efficiently incorporated into the silica skeleton in ZrSBA-15-S, forming acidic Zr–O(H)–Si bridges. These bridges contribute to the enhanced catalytic activity observed in the dehydration and dehydrogenation of 2-propanol. The absence of strong basic sites in ZrSBA-15-S compared to those in Zr/SBA-15-L correlates with the more efficient integration of zirconium into the silica framework, which favors acidic rather than basic catalytic behavior.

Modification of both the zirconium-containing samples with molybdenum species leads to an increase in their catalytic activity, as evidenced by the similar 2-propanol (2-PrOH) conversion achieved at a lower reaction temperature (Fig. 11). The selectivity to the reaction products, however, differs between the zirconium-containing supports and their molybdenum-modified counterparts. A noticeable increase in the selectivity for diisopropyl ether and acetone is observed after the loading of molybdenum onto both Zr/SBA-15-L and ZrSBA-15-S. The formation of acetone is primarily driven by the presence of basic oxygen atoms associated with molyb-

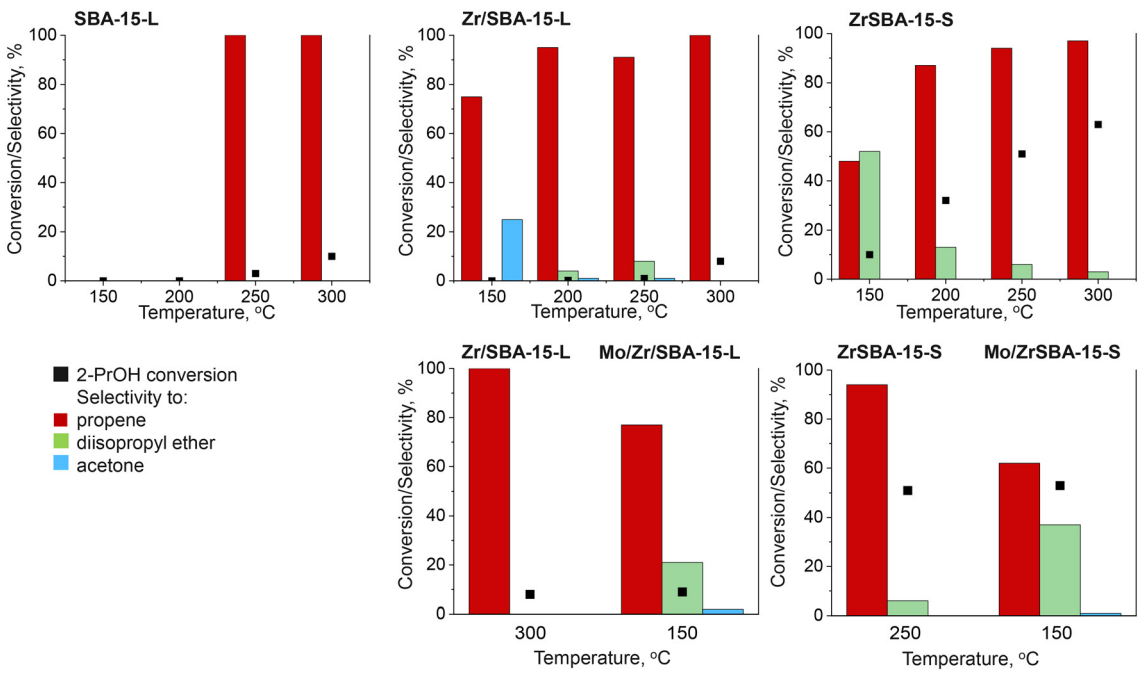

Fig. 11 Results of 2-propanol dehydration and dehydrogenation.

denum species, which facilitate the basic-catalyzed transformation. On the other hand, the formation of diisopropyl ether arises from the interaction between the basic sites from oxygen atoms bonded to molybdenum and the Lewis acid sites (LAS) originating from coordinatively unsaturated molybdenum centers. These centers are formed upon the modification of the Zr/SBA-15-L and ZrSBA-15-S samples with molybdenum species.

The catalysts obtained were also tested in the cyclization and dehydration of 2,5-hexanedione (2,5-HDN), which serves as a model reaction to assess the Brønsted acidity and basicity of the materials. The type of active site is determined by the selectivity observed in this reaction. Specifically, the formation of 2,5-dimethylfuran (DMF) is indicative of the presence of acidic centers, whereas the formation of 3-methyl-2-cyclopentenone (MCP) results from the action of basic sites on the catalyst surface.[57] The product distribution can provide insight into the Brønsted acidity/basicity of the catalysts. A product ratio (MCP/DMF) greater than 1 suggests that the catalyst has a basic character, as the formation of MCP, which is favored by basic sites, predominates. Conversely, if the ratio is lower than 1, the catalyst being acidic in nature is implied, favoring the formation of DMF. A ratio close to 1 indicates that the catalyst exhibits both acidic and basic properties, with a balance between the formation of DMF and MCP.

The results of the cyclization and dehydration of 2,5-hexanedione (2,5-HDN) are presented in Fig. 12. The SBA-15-L sample, which does not contain zirconium or molybdenum species, exhibits basic properties on its surface, consistent with the previous literature data. When zirconium species are incorporated into the silica support to form Zr/SBA-15-L, the conversion of 2,5-HDN increases, while the selectivity remains almost unchanged. This suggests that the number of active sites on the surface has increased due to the introduction of zirconium, enhancing the catalytic activity. Additionally, the molar ratio of MCP/DMF is significantly lower for ZrSBA-15-S compared to that for Zr/SBA-15-L, which indicates that the short-channel silica (ZrSBA-15-S) contains a higher concentration of stronger BAS, which was confirmed by pyridine adsorption measurements. The modification of both the zirconium-containing samples with molybdenum species leads to an increase in both the conversion of 2,5-HDN and the selectivity to DMF. The higher selectivity to DMF is attributed to the increase in the number of stronger BAS on the surface, which is supported by the FT-IR results after desorption of chemisorbed pyridine.

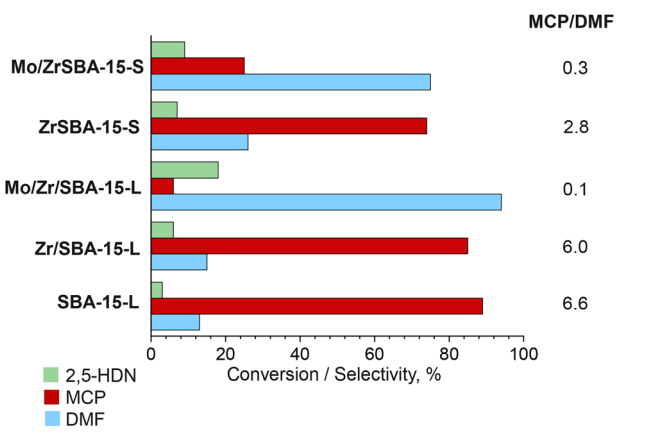

Fig. 12 Results of 2,5-hexanedione cyclization and dehydration at 350 °C.

The activity of the synthesized catalysts was studied using a model mixture of dibenzothiophene (DBT) in *n*-dodecane (with an initial sulfur content of 500 ppm), in the presence of hydrogen peroxide as an oxidizing agent and acetonitrile (ACN) as an extractive solvent. Samples of the reaction mixture were taken from the *n*-dodecane solution at various time intervals, allowing for monitoring of the reaction progress. The results of this reaction are shown in Fig. 13. It should be noted that the reaction product was detected only in the acetonitrile solution, not in the *n*-dodecane phase. This confirms the positive role of the extraction phase in removing sulfone from the oil phase.

The data presented in Fig. 13A show the change in DBT concentration in the oil phase over time. This can be divided into two distinct time regions. In the first region, which covers the initial minutes of the process, very fast removal of DBT is observed (yellow-marked region). As shown in the blank test, the decrease in DBT concentration at the beginning of the process can be attributed to the rapid absorption of sulfur-containing organic compounds into acetonitrile until a certain equilibrium state is reached. After that, the subsequent decrease in DBT concentration in the oil phase depends on the efficiency of DBT oxidation and the adsorption of reaction products (purple-marked region).

The application of SBA-15-L results in the same efficiency of DBT removal as the blank test, which was performed with only hydrogen peroxide and without a catalyst. This is important because it shows that the adsorption of DBT on mesoporous silica does not occur, meaning that the adsorption process on the mesoporous silica surface should not be responsible for DBT removal. The Zr/SBA-15-L and ZrSBA-15-S catalysts show slightly higher DBT removal efficiency than pure silica, but there is no significant difference in DBT concentration in the oil phase during the process. Moreover, DBT removal is slightly higher for ZrSBA-15-S than for Zr/SBA-15-L, especially at the beginning of the process. This correlates with the higher amount of LAS detected in the former material. Therefore, it can be concluded that the two forms of zirconium species postulated in both catalysts, *i.e.*, surface ZrO_2 and Zr incorporated into the silica surface, do not directly interact with hydrogen peroxide to oxidize DBT. As a result, further DBT removal is almost not observed. However, it can be suggested that, unlike pure silica, some DBT may be adsorbed on the surfaces of ZrSBA-15-S and Zr/SBA-15-L, leading to a slight increase in DBT removal compared to the blank test.

After the initial absorption of DBT, an increase in its removal over time is observed for Mo/Zr/SBA-15-L and Mo/

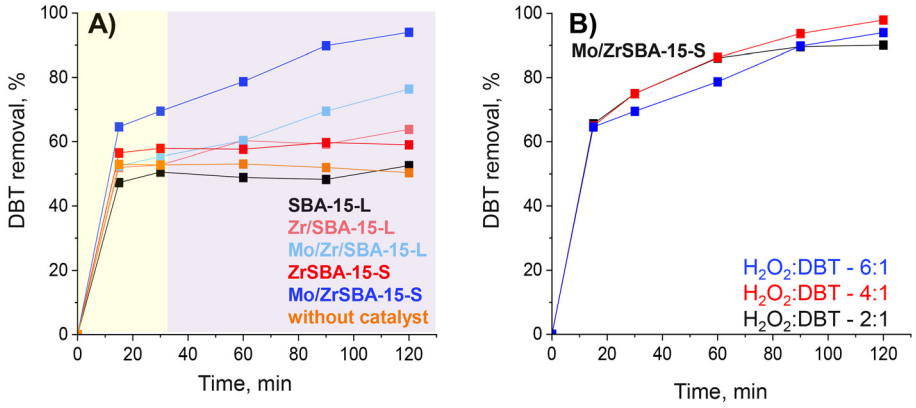

Fig. 13 (A) Activity of the synthesized catalysts in ECODS. Reaction conditions: catalyst: 0.5 wt%, H_2O_2 : DBT – 6 : 1, 60 °C, 120 min, 1000 rpm. (B) Influence of the amount of H_2O_2 on DBT removal. Reaction conditions: catalyst: 0.5 wt%, 60 °C, 120 min, 1000 rpm.

ZrSBA-15-S. The latter sample achieves approximately 94% DBT removal from the oil phase after 2 hours. The lack of DBT oxidation observed for the ZrSBA-15-S sample, which shows the presence of both LAS and BAS, suggests that for effective activation of hydrogen peroxide, the pairing of Lewis acid sites (LAS) with Lewis basic sites (LBS) generated after the immobilization of molybdenum species is responsible for the formation of the peroxo intermediate species that facilitates the effective oxidation of DBT. This intermediate is formed when hydrogen peroxide interacts with the Lewis acid sites, producing electrophilic species capable of promoting efficient oxidative desulfurization of DBT.[58] The visibly higher activity of Mo/ZrSBA-15-S compared to that of Mo/Zr/SBA-15-L in ECODS can be attributed to the migration of electrons from basic sites (from oxygen connected to Mo species) to the bridged Zr–O(H)–Si species, which play the role of strong Brønsted acid sites, as shown in Scheme 1. This process is not observed in Mo/Zr/SBA-15-L, where the presence of ZrO_2 on the silica surface causes the opposite migration of electrons, from the Zr/SBA-15-L support to the pseudo-bridging Si–O(H)–Mo(=O)$_2$ species. The migration of electrons from the Mo(=O)$_2$ species to the bridged Zr–O(H)–Si species in Mo/ZrSBA-15-S increases the number of stronger LAS, as evidenced by pyridine adsorption/desorption measurements. Therefore, the significantly higher efficiency of DBT removal in the presence of Mo/ZrSBA-15-S should be correlated with a higher number of stronger LAS.

Moreover, for the most active sample, Mo/ZrSBA-15-S, the influence of the amount of hydrogen peroxide added to the reaction mixture on DBT removal was examined. The results are shown in Fig. 13B. It is clearly visible that the concentration of hydrogen peroxide does not influence the reaction progress. Based on this, a reuse test was performed with an H_2O_2 : DBT molar ratio of 2, which is more economically beneficial, and the results are presented in Fig. 14. A noticeable decrease in the efficiency of DBT removal for Mo/Zr/SBA-15-L is observed after the third reaction run, and by the fourth reaction run, it is almost the same as for the blank test. Better stability in the ECODS process is observed for Mo/ZrSBA-15-S. This sample shows a slight decrease in DBT removal after the

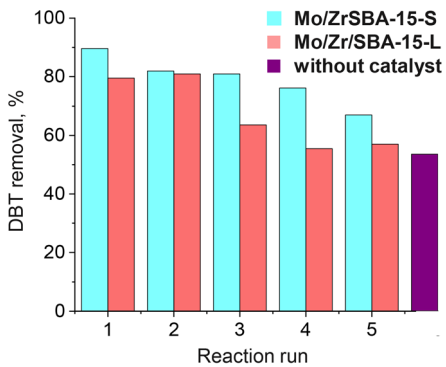

Fig. 14 Stability test of the most active samples in ECODS. Reaction conditions: catalyst: 0.5 wt%, H_2O_2 : DBT – 2 : 1, 60 °C, 90 min, 1000 rpm.

1st and 4th reaction runs; however, its efficiency in DBT removal is still better in the 5th reaction run than that obtained for the blank test. To verify whether leaching of the active phase is responsible for the decrease in DBT removal, XPS measurements were performed after the 5th reaction run of Mo/ZrSBA-15-S. The data presented in Table 1 show that the concentration of surface Zr species is the same before and after the desulfurization processes, whereas the amount of molybdenum species significantly decreased. This confirms that the observed decrease in DBT removal is due to the leaching of molybdenum species. Most probably, in the case of Mo/Zr/SBA-15-L, leaching occurs much faster than for Mo/ZrSBA-15-S. Therefore, the better stability of molybdenum species in Mo/ZrSBA-15-S can likely be correlated with their interaction with the bridged Zr–O(H)–Si species in the support. This highlights the positive role of zirconium species incorporated into the ZrSBA-15-S material.

Table 3 presents a comparison of the catalytic activity in ECODS with hydrogen peroxide acting as the oxidant. This assessment covers and compares Mo/ZrSBA-15-S from the current study and silica-supported catalysts containing molybdenum species as reported in the literature.[1,19,59–61] Mo/

Table 3 Comparison of the activity in DBT removal of supported silicas containing molybdenum species

Catalyst	Catalyst mass, wt%	Solvent	H_2O_2/S	Time, min	Temp., °C	*S* removal, %	Ref.
3%MoO_3/SBA-15	1.2	Hexane	14	60	50	80	59
5%MoO_3/SBA-15	1.2	Hexane	14	60	50	87	59
Mo(10%)/SiO_2	2.0	CH_3CN	8	10	25	99	60
7%Mo/SBA-15	0.25	—	6	60	60	100	1
Mo40-MCM-41	1.0	—	4	120	60	100	19
5%MoO_2/ZrO_2-SiO_2	0.9	MeOH	8	30	25	100	61
Mo/ZrSBA-15-S	0.5	CH_3CN	6	120	60	92	This work

ZrSBA-15-S shows notable proficiency in eliminating DBT from the oil phase, matching the effectiveness of the other catalysts cited.

4. Conclusions

The two different mesoporous silicas, SBA-15 containing zirconium species and exhibiting different morphologies (*i.e.*, plate-like and rod-like), were synthesized and used as support materials for molybdenum species. The obtained catalysts were characterized by several analytical techniques and applied in the extractive catalytic oxidative desulfurization (ECODS) of dibenzothiophene (DBT) in a three-phase system using acetonitrile as a solvent and hydrogen peroxide as an oxidant. Modification of ZrSBA-15-S and Zr/SBA-15-L with molybdenum species did not alter the hexagonal morphology of the supports, and no crystalline molybdenum or zirconium oxides were formed. ZrSBA-15-S exhibited higher acidity than Zr/SBA-15-L due to the introduction of zirconium into the silica skeleton and the formation of bridged Zr–O(H)–Si species, which are the source of Brønsted acid sites (BAS). In the case of Zr/SBA-15-L, zirconium was mainly loaded onto the silica surface in the form of amorphous ZrO_2 particles, which exhibit a stronger basic character. Modification of the zirconium-containing samples with the molybdenum source resulted in the formation of Lewis acid sites (LAS) and BAS in Mo/Zr/SBA-15-L. In contrast, in Mo/ZrSBA-15-S, molybdenum loading caused a decrease in the number of both types of acid sites but increased the strengths of LAS and BAS. The strength of LAS in Mo/ZrSBA-15-S increased due to the migration of electrons from the basic oxygen atom connected to molybdenum to the bridged Zr–O(H)–Si species, whereas the strength of BAS increased as a result of the formation of pseudo-bridging Zr–O(H)–Mo(=O)$_2$ moieties. Consequently, higher molybdenum loading and a higher number of stronger LAS and BAS were observed for Mo/ZrSBA-15-S. The increased number of stronger LAS in Mo/ZrSBA-15-S positively impacted the efficiency of the ECODS process. Moreover, the proven interaction between the Mo and Zr species in Mo/ZrSBA-15-S contributed to the better stability of molybdenum species in this material during the reuse test. The results presented in this study indicate that the short-channel SBA-15 material, prepared without the removal of zirconium species, could be an interesting support for other active components.

Author contributions

Katarzyna Stawicka: conceptualization, data curation, formal analysis, investigation, methodology, project administration, supervision, validation, visualization, writing – original draft, and writing – review and editing. Aleksandra Rybka: investigation. Maria Ziolek: conceptualization, funding acquisition, resources, and writing – review and editing. Maciej Trejda: conceptualization, methodology, resources, writing – original draft, and writing – review and editing.

Data availability

We would like to declare that all relevant data related to the manuscript are presented in the main text.

Conflicts of interest

There are no conflicts to declare.

Acknowledgements

The National Science Centre in Poland (Project No. UMO-2018/29/B/ST5/00137) is gratefully acknowledged for its financial support.

References

1 A. Akopyan, P. Polikarpova, O. Gul, A. Anisimov and E. Karakhanov, *Energy Fuels*, 2020, **34**, 14611–14619.
2 A. A. Alghamdi, Y. M. Mrair, F. A. Alharthi and A. B. Al-Odayni, *Appl. Sci.*, 2020, **10**, 5835–5848.
3 V. Chaudhary and S. Sharma, *J. Porous Mater.*, 2016, **24**, 741–749.
4 X. Feng, M. Yan, T. Zhang, Y. Liu and M. Bao, *Green Chem.*, 2010, **12**, 1758–1766.
5 J. P. Thielemann, T. Ressler, A. Walter, G. Tzolova-Müller and C. Hess, *Appl. Catal., A*, 2011, **399**, 28–34.
6 G. Wang, L. Zhang, J. Deng, H. Dai, H. He and C. T. Au, *Appl. Catal., A*, 2009, **355**, 192–201.
7 J. Wisniewska, K. Grzelak, S. P. Huang, I. Sobczak, C. M. Yang and M. Ziolek, *Catal. Today*, 2020, **356**, 165–177.

8 F. Li, J. G. Wang, Y. P. Liu, H. J. Zhou and T. H. Chen, *J. Mater. Sci.*, 2009, **44**, 6505–6511.
9 F. E. da Silva, E. Rigoti, M. I. Soares de Mello and S. B. C. Pergher, *Materials*, 2024, **17**, 2827–2841.
10 S. Y. Chen, C. Y. Tang, W. T. Chuang, J. J. Lee, Y. L. Tsai, J. C. Chan, C. Y. Lin, Y. C. Liu and S. Cheng, *Chem. Mater.*, 2008, **20**, 3906–3916.
11 K. Pei-Hsin, H. Chen-Yun, C. Mei-Jing, L. Tai-Hsuan, L. Yi-Tian, L. Szu-Chieh, T. Kea-Tiong, Y. Da-Jeng and Y. Chia-Min, *Langmuir*, 2012, **28**, 11639–11645.
12 R. Ghubayra, R. Yahya, E. F. Kozhevnikova and I. V. Kozhevnikov, *Fuel*, 2021, **301**, 121083–121090.
13 M. A. Betiha, A. M. Rabie, H. S. Ahmed, A. A. Abdelrahman and M. F. El-Shahat, *Egypt. J. Pet.*, 2018, **27**, 715–730.
14 A. Rajendran, T. Y. Cui, H. X. Fan, Z. F. Yang, J. Feng and W. Y. Li, *J. Mater. Chem. A*, 2020, **8**, 2246–2285.
15 P. Polikarpova, A. Akopyan, A. Shlenova and A. Anisimov, *Catal. Commun.*, 2020, **146**, 106123–106140.
16 A. Nurwita and M. Trejda, *Int. J. Mol. Sci.*, 2023, **24**, 16957–16968.
17 Y. Wang, F. Du, C. Wang, J. Zhao, H. Sun and C. Sun, *J. Chem. Res.*, 2022, **46**, 1–8.
18 L. P. Rivoira, B. C. Ledesma, J. M. Juárez and A. R. Beltramone, *Fuel*, 2018, **226**, 498–507.
19 P. Polikarpova, A. Akopyan, A. Shigapova, A. Glotov, A. Anisimov and E. Karakhanov, *Energy Fuels*, 2018, **32**, 10898–10903.
20 G. Estephane, C. Lancelot, P. Blanchard, V. Dufaud, S. Chambrey, N. Nuns, J. Toufaily, T. Hamiye and C. Lamonier, *Appl. Catal., A*, 2019, **571**, 42–50.
21 Y. Chen, Q. Tian, Y. Tian, J. Cui and G. Wang, *Appl. Sci.*, 2021, **11**, 1–15.
22 A. Teimouri, M. Mahmoudsalehi and H. Salavati, *Int. J. Hydrogen Energy*, 2018, **43**, 14816–14833.
23 L. P. Rivoira, J. Cussa, M. L. Martínez and A. R. Beltramone, *Catal. Today*, 2020, **349**, 68–80.
24 Y. Wang, G. Zhang, T. Guan, F. Xu, J. Wu, E. Zhou, J. Wang and K. Li, *ChemistrySelect*, 2020, **5**, 2148–2156.
25 J. M. Ramos, J. A. Wang, S. O. Flores, L. Chen, U. Arellano, L. E. Noreña, J. González and J. Navarrete, *Catalysts*, 2021, **11**, 408–429.
26 K. Stawicka, M. Gierada, J. Gajewska, F. Tielens and M. Ziolek, *Appl. Surf. Sci.*, 2020, **513**, 145802–145812.
27 C. A. Emeis, *J. Catal.*, 1993, **141**, 347–354.
28 K. A. Cychosz and M. Thommes, *Engineering*, 2018, **4**, 559–566.
29 M. Thommes, K. Kaneko, A. V. Neimark, J. P. Olivier, F. Rodriguez-Reinoso, J. Rouquerol and K. S. W. Sing, *Pure Appl. Chem.*, 2015, **87**, 1051–1069.
30 M. Trejda, D. Kryszak and M. Ziolek, *Mater. Res. Bull.*, 2018, **97**, 530–536.
31 K. Grzelak, I. Sobczak, C. M. Yang and M. Ziolek, *Catal. Today*, 2020, **356**, 155–164.
32 X. Wang, K. S. K. Lin, J. C. C. Chan and S. Cheng, *Chem. Commun.*, 2004, **2**, 2762–2763.
33 M. Trejda, M. Ziolek, P. Decyk and D. Duczmal, *Microporous Mesoporous Mater.*, 2009, **120**, 214–220.
34 J. Iglesias, J. A. Melero, L. F. Bautista, G. Morales, R. Sánchez-Vázquez, M. T. Andreola and A. Lizarraga-Fernández, *Catal. Today*, 2011, **167**, 46–55.
35 M. Olejniczak and M. Ziolek, *Microporous Mesoporous Mater.*, 2014, **196**, 243–253.
36 H. Li, M. Zhang, J. Liu, J. Yang, X. Chen, M. Wang, H. Li and W. Zhu, *Inorg. Chem. Front.*, 2019, **6**, 451–458.
37 N. Maheswari and G. Muralidharan, *Appl. Surf. Sci.*, 2017, **416**, 461–469.
38 M. Wei, K. Okabe, H. Arakawa and Y. Teraoka, *Catal. Commun.*, 2004, **5**, 597–603.
39 M. A. Gondal, T. A. Fasasi, U. Baig and A. Mekki, *J. Nanosci. Nanotechnol.*, 2017, **18**, 4030–4039.
40 A. Gervasini, L. Wahba, M. D. Finol and J.-F. Lamonier, *Mater. Sci. Appl.*, 2012, **03**, 195–212.
41 Z. Li, L. Gao and S. Zheng, *Mater. Lett.*, 2003, **57**, 4605–4610.
42 C. Tagusagawa, A. Takagaki, A. Iguchi, K. Takanabe, J. N. Kondo, K. Ebitani, T. Tatsumi and K. Domen, *Catal. Today*, 2011, **164**, 358–363.
43 M. Baltes, A. Kytökivi, B. M. Weckhuysen, R. A. Schoonheydt, P. Van Der Voort and E. F. Vansant, *J. Phys. Chem. B*, 2001, **105**, 6211–6220.
44 K. Stawicka, M. Trejda and M. Ziolek, *Microporous Mesoporous Mater.*, 2013, **181**, 88–98.
45 N. Scotti, S. Borsacchi, S. Monti, A. Zimina, C. Evangelisti, M. Geppi, P. Dambruoso, G. Barcaro, F. Bossola, V. Dal Santo and N. Ravasio, *J. Alloys Compd.*, 2024, **992**, 174545–174554.
46 L. F. Chen, L. E. Noreña, J. Navarrete and J. A. Wang, *Mater. Chem. Phys.*, 2006, **97**, 236–242.
47 K. Amakawa, Y. Wang, J. Kröhnert, R. Schlögl and A. Trunschke, *Mol. Catal.*, 2019, **478**, 110580–110588.
48 K. Shen, X. Liu, G. Lu, Y. Miao, Y. Guo, Y. Wang and Y. Guo, *JJ. Mol. Catal. A:Chem.*, 2013, **373**, 78–84.
49 K. Hadjiivanov, *Identification and Characterization of Surface Hydroxyl Groups by Infrared Spectroscopy*, 2014, vol. 57.
50 E. Guglielminotti, *Langmuir*, 1990, **6**, 1455–1460.
51 V. Blausäure and A. Acetonitril.
52 L. E. Davies, N. A. Bonini, S. Locatelli and E. E. Gonzo, *Lat. Am. Appl. Res.*, 2005, **35**, 23–28.
53 S. T. Korhonen, M. Calatayud and A. O. I. Krause, *J. Phys. Chem. C*, 2008, **112**, 6469–6476.
54 P. Hoffmann and E. Knozinger, *Surf. Sci.*, 1987, **188**, 181–198.
55 A. Gervasini, J. Fenyvesi and A. Auroux, *Catal. Lett.*, 1997, **43**, 219–228.
56 A. P. Kumar and J. H. Park, *Anal. Lett.*, 2012, **45**, 15–42.
57 R. M. Dessau, *Zeolites*, 1990, **10**, 205–206.
58 M. A. Astle, G. A. Rance, H. J. Loughlin, T. D. Peters and A. N. Khlobystov, *Adv. Funct. Mater.*, 2019, **29**, 1–10.
59 F. Bibak and G. Moradi, *React. Kinet., Mech. Catal.*, 2020, **131**, 935–951.
60 K. P. Gevorgyan, V. I. Larionov, A. V. Akopyan, A. V. Anisimov and P. D. Domashkina, *ACS Omega*, 2024, **9**, 13831–13839.
61 P. Zhang, Y. Tong, M. Zhu and B. Dai, *New J. Chem.*, 2020, **44**, 3786–3793.

